

Spatial Transcriptomics-Based Identification of Molecular Markers for Nanomedicine Distribution in Tumor Tissue

Jeongbin Park, Jinyeong Choi, Jae Eun Lee, Hongyoon Choi,* and Hyung-Jun Im*

The intratumoral accumulation of nanomedicine has been considered a passive process, referred to as the enhanced permeability and retention effect. Recent studies have suggested that the tumor uptake of nanomedicines follows an energy-dependent pathway rather than being a passive process. Herein, to explore the factor candidates that are associated with nanomedicine tumor uptake, a molecular marker identification platform is developed by integrating microscopic fluorescence images of a nanomedicine distribution with spatial transcriptomics information. When this approach is applied to PEGylated liposomes, molecular markers related to hypoxia, glycolysis, and apoptosis can be identified as being related to the intratumoral distribution of the nanomedicine. It is expected that the method can be applied to explain the distribution of a wide range of nanomedicines and that the data obtained from this analysis can enhance the precise utilization of nanomedicines.

molecules to ensure better therapeutic efficacy.^[4] In 1995, Doxil, a doxorubicin-loaded PEGylated liposome, was approved by the U.S. Food and Drug Administration (FDA) and became the first nanomedicine approved for clinical use.^[5] Currently, there are approximately two dozen FDA-approved nanomedicines, including lipid-based, polymer-based, and iron-oxide-based nanoparticles.^[4]

Generally, nanomedicines have a size range of 10–150 nm and demonstrate significantly different pharmacokinetics compared to conventional small-molecule drugs.^[6] Unlike small-molecule drugs, nanomedicines are not freely diffusible into tissues and tend to reside in the vascular space after intravenous administration. In most cases, nanomedicines are removed from circulation through opsonization

by serum proteins followed by phagocytosis by the reticuloendothelial system (RES). Various surface modification methods, including PEGylation and the introduction of self-peptides, have been introduced to delay opsonization and thus prolong circulation times. By prolonging the circulation time of nanomedicines, the delivery efficiency can be enhanced. This enhanced delivery of nanomedicines realized by prolonged circulation times is clearly seen in diseased tissue, such as tumors or inflammatory regions, but is not prominent in normal tissues.^[7] This phenomenon is called enhanced permeability and retention (EPR) and has become a major theory explaining the improved delivery

1. Introduction

Nanomedicines hold great promise to improve disease diagnoses and treatments in those with various illnesses, including cancer,^[1] immunological diseases,^[2] and infectious diseases.^[3] Nanomedicine is developed based on nanotechnology and has several advantages over conventional drug platforms. First, it is capable of loading imaging contrast for enhanced diagnostic imaging. Second, surface modifications and decorations of targeting moieties for enhanced drug delivery are possible. Finally, it is relatively simple to load various types of treatment

J. Park, H.-J. Im
Department of Molecular Medicine and Biopharmaceutical Sciences
Graduate School of Convergence Science and Technology
Seoul National University
Seoul 08826, Republic of Korea

J. Choi, H.-J. Im
Department of Applied Bioengineering
Graduate School of Convergence Science and Technology
Seoul National University
Seoul 08826, Republic of Korea

J. E. Lee
Portrai Inc
Seoul 03136, Republic of Korea

H. Choi
Department of Nuclear Medicine
Seoul National University College of Medicine
Seoul 03080, Republic of Korea
E-mail: chy1000@snu.ac.kr

H. Choi
Department of Nuclear Medicine
Seoul National University Hospital
Seoul 03080, Republic of Korea

H.-J. Im
Cancer Research Institute
Seoul National University
Seoul 03080, Republic of Korea
E-mail: iiijhjj@snu.ac.kr

H.-J. Im
Research Institute for Convergence Science
Seoul National University
Seoul 08826, Republic of Korea

 The ORCID identification number(s) for the author(s) of this article can be found under <https://doi.org/10.1002/smt.202201091>.

DOI: 10.1002/smt.202201091

efficiency of nanomedicines compared to conventional small-molecule drugs. The EPR effect was considered a passive process due to leaky neovascularization and limited lymphatic drainage in diseased tissues compared to normal tissues.^[8]

Recently, the notion that enhanced tumor accumulation of nanomedicines is a passive process has been challenged. An *in vivo* imaging study based on biodistribution analysis using radiolabeled PEGylated liposomes showed that markers for blood and lymphatic vessel density were not significantly associated with the tumor accumulation levels, in contrast to the prior hypothesis.^[9] Furthermore, the quantified number of endothelial gaps in tumor vasculature is too low to explain the tumor accumulation of the nanoparticles and 97% of the nanoparticles accumulate in the tumor via an active process according to the simulation.^[10] However, it is very challenging to identify markers that govern active process of the nanomedicine tumor accumulation. So far, only a few potential RNA or protein markers can be analyzed by immunohistochemistry (IHC) or reverse transcription polymerase chain reaction (RT-PCR).^[9,11] The next-generation sequencing (NGS) technology now can provide an unbiased exploration of the molecular markers. Since tumor uptake of nanoparticles is heterogeneous within the tumor,^[12] it is difficult to find factors that determine nanoparticle uptake by conventional RNA sequencing method that obtains the average value of gene expression in the tissue without spatial information.^[13]

Recent technological advances have established spatial transcriptomics (ST) that can systematically identify the expression levels of all genes throughout the tissue space.^[14] Because ST data inherently possesses spatial information, it can be easily integrated with other types of imaging data and is considered most appropriate for analyzing spatially heterogeneous information within tissues.^[14b] Meanwhile, it is easily possible to determine the distribution of nanomedicines within the tumor by using fluorescently labeled nanomedicines.^[15] Therefore, we hypothesized that molecular factors related to heterogeneous

nanomedicine tumor uptake can be identified by the integration of ST data and fluorescent imaging in cancer tissue after the injection of a fluorescently labeled nanomedicine.

2. Results and Discussion

2.1. In Vivo and Ex Vivo Fluorescence Imaging of a Mouse Syngeneic Tumor

In this study, a PEGylated liposome was selected as a model nanomedicine, as these liposomes are undoubtedly among the most successful nanomedicine platforms. Also, factors determining the high uptake of PEGylated liposomes remain controversial, as noted in the previous study.^[16] To select an ideal form of PEGylated liposomes, we synthesized four different types of PEGylated liposomes, which are large less PEGylated liposome (LLP), large highly PEGylated liposome (LHP), small less PEGylated liposome (SLP), and small highly PEGylated liposome (SHP) (Figure S1A, Supporting Information). We intravenously injected the nanoparticles to 4T1 tumor-bearing mice ($n = 3$ for each group) and obtained *in vivo/ex vivo* fluorescence imaging using an *in vivo* fluorescence imaging system (IVIS). We found that highly PEGylated liposomes demonstrated higher tumor uptake compared to less PEGylated liposomes and there was no significant difference between large and small PEGylated liposomes (Figure S1B,C, Supporting Information). In addition, polydispersity index (PDI) of LHP was slightly smaller than that of SHP, therefore, we chose LHP for further experiments and described LHP as PEGylated liposomes. Transmission electron microscopy (TEM) images of PEGylated liposomes showed a uniform and round shape, allowing the identification of a typical lipid bilayer of liposomes. The hydrodynamic sizes of the fluorescent liposomes were 291.73 ± 8.81 nm. The maximum absorbance wavelength was 550 nm and the maximum emission wavelength at 550 nm excitation was 563 nm (Figure 1A).

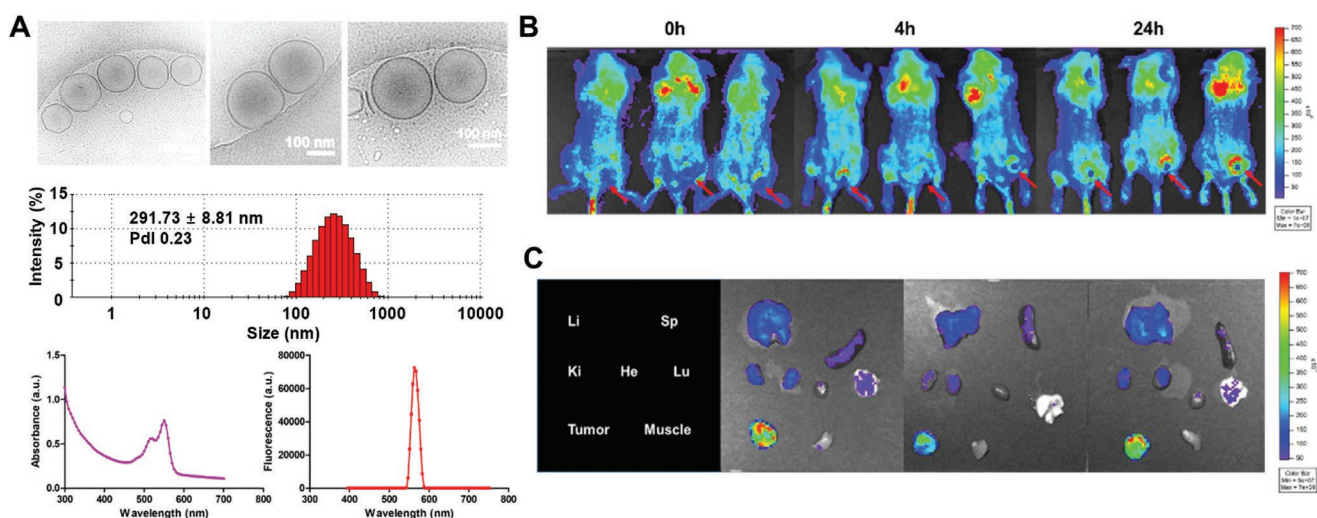


Figure 1. Fluorescence imaging of DiI-loaded liposomes. A) The characterization profile of DiI-loaded liposome using transmission electron microscopy (TEM), dynamic light scattering instrument (DLS), and microplate reader. The DLS result was expressed by mean size \pm SD. B) *In vivo* fluorescence imaging of 0, 4, and 24 h after intravenous injection in 4T1 breast tumor model. C) *Ex vivo* fluorescence imaging of main organs (liver, spleen, kidneys, heart, lung, tumor, and muscle).

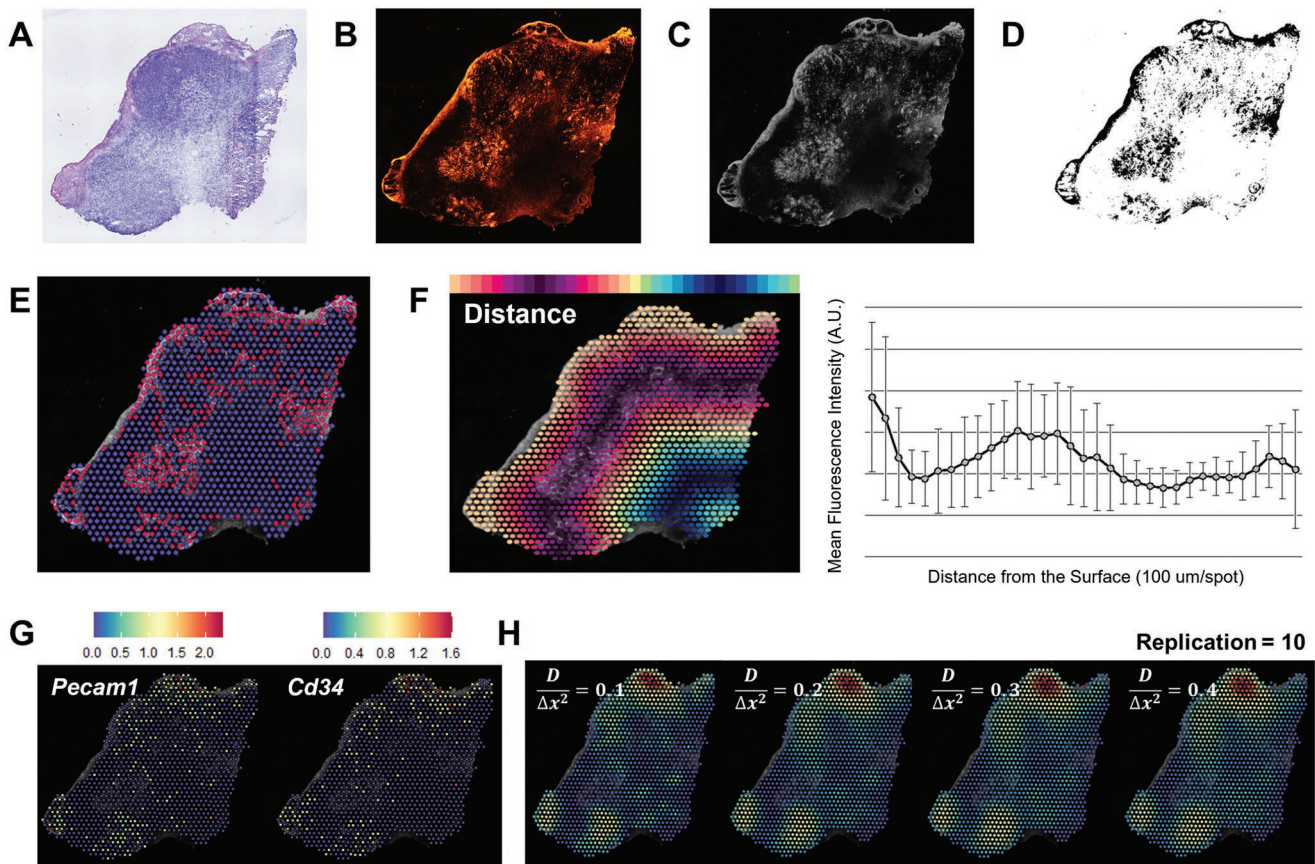


Figure 2. Tumor sections and initial exploration of data. A) H&E staining image representing the overall histological features. A serial process beginning from original fluorescence image included B) fluorescence image normalization, C) image registration, D) image binarization, and E) acquiring binary map corresponded to the binary image. F) A map colored by the distance from the left-most surface region and the average fluorescence intensity according to the distance. The values were expressed by mean \pm SD. G) Spatial feature plots of *Pecam1* and *Cd34* and H) simulation results of Fick's diffusion annotated by C/k with different $D/\Delta x^2$ values.

We observed that PEGylated liposomes accumulated in the 4T1 tumor in all three mice tested (Figure 1B). Also, ex vivo fluorescence imaging of normal organs and tumors were obtained 24 h after the injection (Figure 1C). Fluorescent signals were observed mainly in the tumors and livers. Also, minimal fluorescence signals can be seen in kidneys, spleen, and lungs. The biodistribution pattern of the fluorescent liposomes was similar to the previously reported biodistribution of PEGylated liposomes in tumor-bearing mice.^[17]

2.2. H&E Staining, Spatial Transcriptomics, and Fluorescence Imaging of the Tissue

Among the three excised tumors, the tumor with the highest fluorescent signal was selected for further experiments. We obtained two consecutive sections from the tumor, and the one section was used for hematoxylin and eosin (H&E) staining and ST analysis (Figure 2A), and the other was used for fluorescence imaging (fluorescent liposome distribution map) (Figure 2B). Spatial mapping of RNA reads indicated a cancer-rich region that showed the highest gene expression, with the necrotic region, the lower and right part of the tissue, showing

the lowest (Figure S2, Supporting Information). According to the fluorescence image, the fluorescent signal was prominent in the tumor capsule area, with multiple foci of increased fluorescent signal found in the inner region of the tissue. Next, we obtained a binary map of the fluorescence image, and the map was matched with ST spots for further analyses (Figure 2B–E). The pattern of the average fluorescence intensity according to the distance from the surface was different from the mathematical model for simple passive diffusion (Figure 2F). The numerical analysis results of Fick's law were obtained to predict the passive process of fluorescent liposome distribution using the vascular marker, *Pecam1*. The distribution did not concur with the actual fluorescent liposome distribution and especially could not explain the intratumoral uptake of nanoparticles. This was the same with another representative pan-endothelial marker, *Cd34* (Figure 2B,G,H; and Figure S3, Supporting Information).

2.3. *Hbb-bs* was Partially Related to the Fluorescence Liposome Distribution

First, we derived differentially expressed genes (DEGs) related to the high accumulation of fluorescent liposomes in the tumor

section by comparing high versus low uptake spots using binary fluorescence imagery. We found that there was only one significant gene, *Hbb-bs* (Figure 3A; and Table S1, Supporting Information). *Hbb-bs* encodes a beta polypeptide chain found in hemoglobin in red blood cells (RBCs) and considered as one of the RBC markers.^[18] Consistently, we found that the expressions of vascular markers (e.g., *Pecam1*, *Cd34*) were similar to the distribution of *Hbb-bs*. This result implied that the fluorescent liposome distribution is partially associated with blood circulation (Figure 3A).

We determined the principal components (PC1, PC2, and PC3) in the fluorescent image of the tumor tissue by using spatial gene expression patterns by deep learning of tissue images (SPADE) algorithm.^[19] The most variable latent feature of the fluorescence image (i.e., PC1) showed a pattern similar to that of the distribution of fluorescent liposomes (Figure 3B). We obtained PC1-associated genes (SPADE genes) and demonstrated them using enhanced volcano plots (Figure 3C). Among the SPADE genes, it is noteworthy that *Ctsk*, *Lbp*, *Sparcl1*, and *Apod* were high-ranked and up-regulated genes, which are abundant in the extracellular matrices (ECMs) of the stromal region (Figure 3D; and Table S2, Supporting Information). This finding is in line with the previous observation that nanoparticle tumor uptake is associated with capillary wall collagen.^[11] Also, it is well known that *Apod* can be found in the early stage of tumor development among the apolipoproteins, consistent with the present experimental condition.^[20] The SPADE genes were associated with regulation of smooth muscle cell proliferation and fibronectin binding according to the gene ontology analysis (Figure 3E). To further investigate the association between the expression of *Hbb-bs* and the nanomedicine distribution, we conducted a correlation analysis of the fluorescent signal intensity and the expression level of *Hbb-bs* within high-uptake spots. There was no statistically significant correlation between *Hbb-bs* expression level and fluorescence intensity ($r = 0.073$, p -value = 0.188). It means that *Hbb-bs* was shown only to reflect the environment of peripheral accumulation of nanoparticles, but not a key player to govern the uptake of nanoparticles.

2.4. Division of Uptake Pattern Clusters and Cell Type Analysis

Hbb-bs and SPADE genes were found to be partially related to the fluorescent distribution of nanomedicines in the tissue. However, the expression pattern of the genes did not match the inner uptake clusters of the tumor (Figures 2B vs 3A,D). We speculated that the nanoparticle (NP) uptake mechanisms on the surface and in the inner area of the tumor could differ, therefore the uptake patterns were analyzed using image feature-based clusters. The regions of fluorescent image were clustered using a CNN-based features based on tiles of the image and K-means clustering. K was set to 4 as the minimum requirement for the division of the peripheral area from the inner area (Figure S4, Supporting Information). Also, we obtained two clusters of high-uptake spots (cluster 1: surface cluster, cluster 2: inner cluster) by matching the regions with the binary map (Figure 4A). Through the unsupervised hierarchical clustering of spots in cluster 1 and 2, outliers were

defined as incoherent spots between the uptake pattern clusters and the newly formed clusters and eliminated for further analyses (Figure S5, Supporting Information).

We then analyzed the cell distribution of the clusters using three different types of cell-type prediction methods: multimodal intersection analysis (MIA),^[21] robust cell type decomposition (RCTD),^[22] and domain adaptation-based cell type inference in spatial transcriptomic data (CellDART).^[23] Using MIA, fibroblasts and endothelial cells were preferentially discovered in cluster 1, while cancer cells were found to be predominant in cluster 2 (Figure 4B). In the RCTD analysis, cancer cells were dominant in both clusters and endothelial cells and fibroblasts were the major cell types in cluster 1 (Figure 4C). We could confirm the relatively dominant distributions of endothelial cells and fibroblasts in cluster 1 compared to cluster 2, an outcome similar to the results of the MIA analysis. Results of CellDART verified the observations from the MIA analysis and RCTD assessment (Figure 4D). Cancer cells are dominant in the tumor tissue while endothelial cells and fibroblasts are clearly observed in the surface region of the tumor according to CellDART. Also, the presence of inflammatory macrophages from the MIA assay and the dominance of cancer cells in the RCTD assay were reflected in the CellDART results.

2.5. Identification of DEGs and Uptake-Associated Genes in Cluster 1 and 2

We conducted DEG analysis of cluster 1 and 2 by comparing cluster 0 versus 1 and 0 versus 2, respectively. Volcano plots of DEGs showed different genetic profiles between cluster 1 and 2 (Figure 5A,B; and Tables S3 and S4, Supporting Information). In addition, a dot plot representing the top 20 DEGs for each cluster verified the uniqueness of each cluster (Figure 5C). DEGs of cluster 1 were similar to the result of the previous analysis using the entire tissue slide. For example, we could observe RBC markers such as *Hbb-bs*, *Hba-a1*, and *Hba-a2* and stromal genes such as *Apod*, *Aqp1*, *Col3a1*, *Gpx3*, *Apoe*, and *Sparcl1* among the top 20 DEGs in cluster 1 (Table S3, Supporting Information).

The DEGs in cluster 1 showed no significant correlation with the fluorescent signal (Figure 5D). On the other hand, there were a total of 31 genes that were upregulated and positively correlated with fluorescence intensity in cluster 2 (Figure 5D; and Figure S6 and Table S5, Supporting Information). These genes were associated with three representative physiological functions of cancer in gene ontology: hypoxia, glycolysis, and apoptosis (Figure 5E; and Table S5, Supporting Information). When plotting the scores of three gene ontology (GO) terms, the spatial distribution of the scores were all colocalized (Figure 5F), and the distribution was similar to the internal distribution of the nanoparticles (Figure 2B).

The DEGs from the clusters may simply be region-associated genes because the spots in the clusters are spatially close. However, we speculated that the DEGs having statistically significant correlations with fluorescence intensity within the cluster are truly associated with nanomedicine uptake process. Several previous studies have reported that a hypoxic condition can

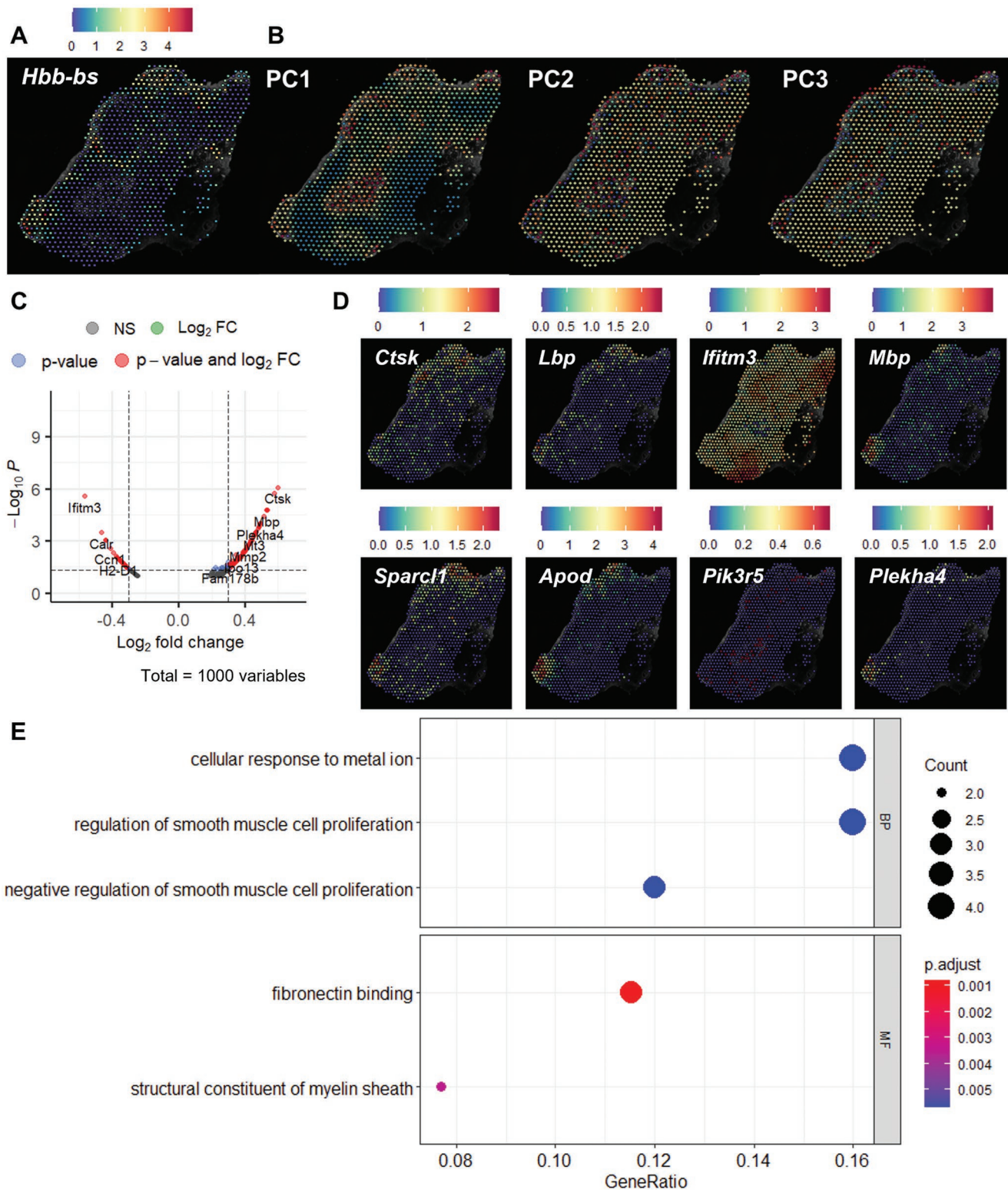


Figure 3. Results of overall fluorescence analysis. A) A spatial feature plot of the only differentially expressed gene (DEG), *Hbb-bs*. B) Image latent features generated by SPADE algorithm. PC1, PC2, and PC3 referred to principal component 1, and so on. C) Enhanced volcano plot with top 1000 variable genes. D) Spatial feature plots of top 8 SPADE genes with highest fold change (FC). E) GO analysis for PC1 SPADE genes of top 30 up-regulated genes according to biological process (BP), cellular component (CC), and molecular function (MF). Top 3 positive GO terms for each category were considered and *p* values were adjusted by B&H method.

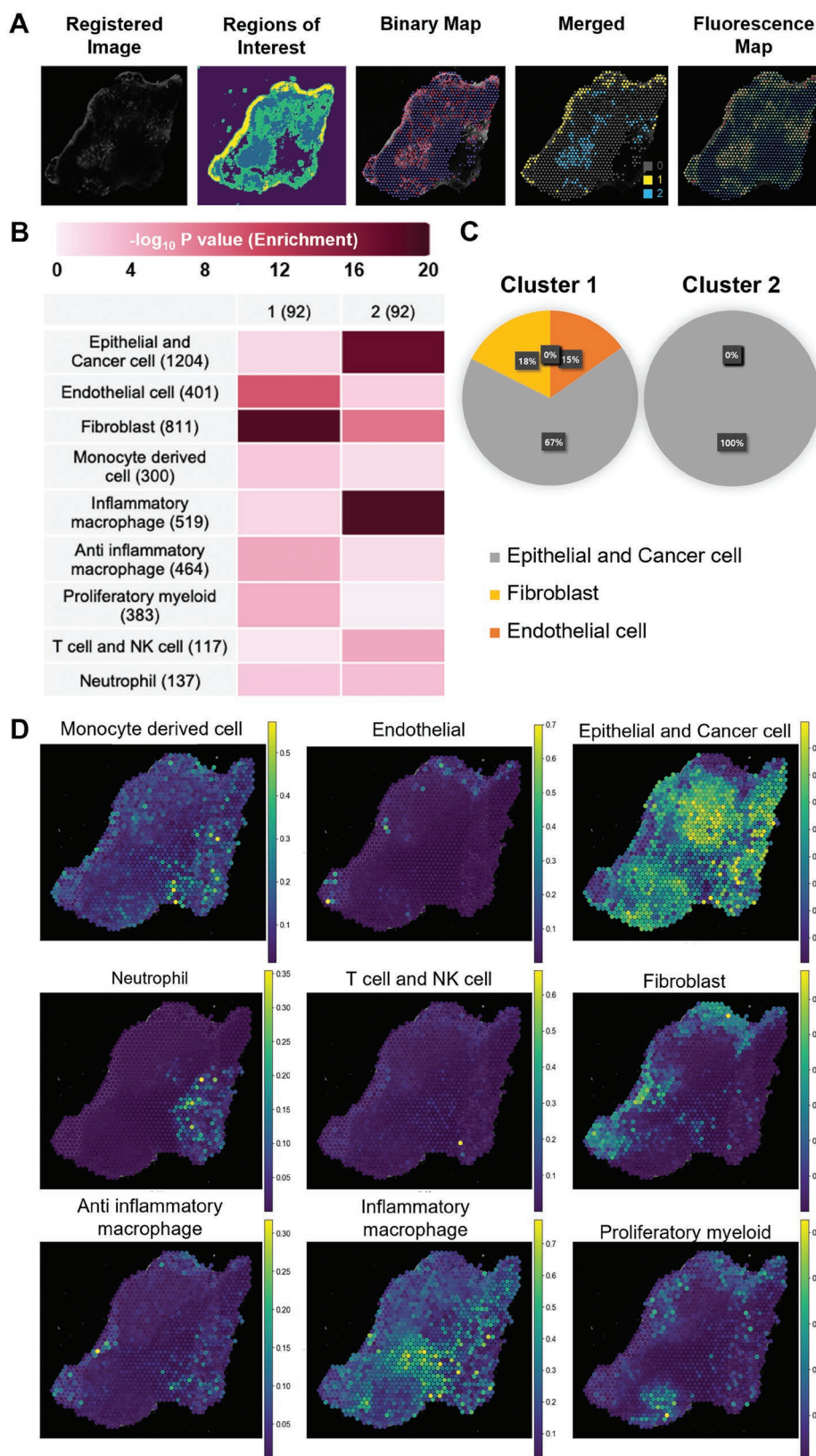


Figure 4. Results of subgroup fluorescence analysis. A) A process determining uptake clusters beginning from registered fluorescence image. B) MIA analysis for cluster 1 and 2. p values were acquired by using hypergeometric cumulative distribution and were represented by the color bar. C) Results of cell type population derived from RCTD algorithm. D) Spatial feature plots representing each cell type occurrence acquired from the results of Cell-DART algorithm. In each spot, the sum of the occurrences of all cell types is 1.

enhance NP uptake in cancer cells.^[24] According to our unbiased methods, markers related to hypoxia can be identified to be associated with the PEGylated liposome tumor distribution. We found that one of the most important glycolysis mediator genes, *Pfkfb*, appeared to be an uptake-associated gene in cluster 2, as well (Tables S4 and S5, Supporting Information). It is well known that a hypoxic condition in cancer tissue enhances the glycolysis of cancer cells.^[25] Also, a previous study showed that a significant correlation existed between the degree of hypoxia and glucose metabolism as assessed by in vivo positron emission tomography (PET) in patients' tumors.^[26] Because a lack of energy generation is prevalent in cancer cells due to the low efficiency of hypoxic metabolism, starvation-induced apoptosis can be triggered.^[27] Also, molecular markers related to lipid metabolism were found to be uptake-associated genes. Hypoxia can reprogram a number of genes related to energy metabolism. In recent years, a link between hypoxia and lipid metabolism was also revealed. In particular, endocytosis of lipoproteins is enhanced by the upregulation of lipoprotein receptor-related protein (LRP1)^[28] and very-low-density lipoprotein receptor (VLDLR).^[29] Thus, we speculated that several hypoxia-induced metabolism-related genes, such as *Ndr1*, which participates in low-density lipoprotein receptor trafficking and lipid metabolism, play an important role in the uptake of PEGylated liposomes. *Plin2*, one of the DEGs in cluster 2 may also be linked to this speculation, as the gene is involved in the hypoxia-inducible lipid droplet-associated protein with Hif-1 α . Meanwhile, we conducted a correlation analysis of the uptake-associated genes to find an association between each pair of genes (Figure S7, Supporting Information). Most of the genes were clustered

as set a-1, a-2, and a-3, which are correspondingly related to "hypoxia + glycolysis," "hypoxia + apoptosis," and "apoptosis only." Also, a heatmap indicated that most genes showed strong connectivity, possibly due to a common biological context, except for the three genes in set b.

2.6. Validation of Uptake-Associated Genes

Immunofluorescence (IF) experiments were performed in tumor tissues from four different 4T1 tumor-bearing mice to see if the marker expressions at protein level can reflect the intratumoral distribution of PEGylated liposomes. Anti-Vdac1 antibody was prepared for IF as the correlation coefficient with the gene and the nanoparticle uptake was the highest among uptake-associated genes in cluster 2. Anti-Pecam1 antibody was also prepared because it is a marker for tumor angiogenesis,^[30] which has been thought to be a major factor to drive the uptake of nanoparticles according to the passive pathway of EPR effect.^[8a] When fluorescence signals from IF and PEGylated liposome was compared, the PEGylated liposome uptake pattern was more concurred with IF using anti-Vdac1 antibody compared to that using anti-Pecam1 antibody in all four samples. In addition, we performed correlation analysis between the fluorescence signals of the PEGylated liposome and the IF images using the antibodies, the correlation coefficient between PEGylated liposome and Vdac1 was significantly higher than that between PEGylated liposome and Pecam1 (p -value = 0.01) (Figure 6).

To verify reproducibility and robustness of ST analysis from the first sample (Sample A-1), two more ST datasets were acquired: one from the same tumor tissue (Sample A-2) and

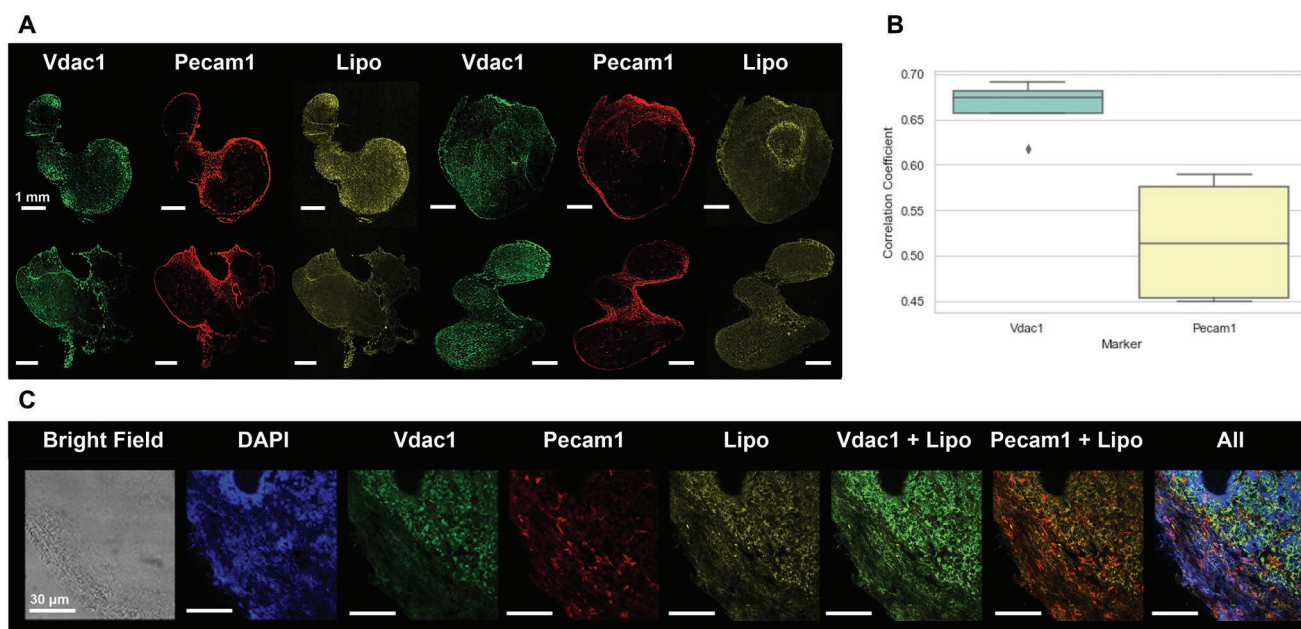


Figure 6. Results of IF validation study. A) Liposome fluorescence images and IF images of anti-Vdac1 primary antibody and anti-Pecam1 primary antibody from 4 different 4T1 tumor tissues. B) Pearson correlation analysis between the IF images of antibodies and the fluorescent liposome distributions. The correlation coefficient between the IF images of anti-Vdac1 antibody and the liposome fluorescence images was 0.66 ± 0.03 ; on the other hand, the correlation coefficient between the IF images of anti-Pecam1 antibody and the liposome fluorescence images was 0.52 ± 0.07 . One-way ANOVA between the two showed a p -value of 0.01, rejecting the null hypothesis that there is no difference between the two. C) Local IF results showing that anti-Vdac1 antibody is a better indicator of fluorescent liposome distribution than anti-Pecam1 antibody.

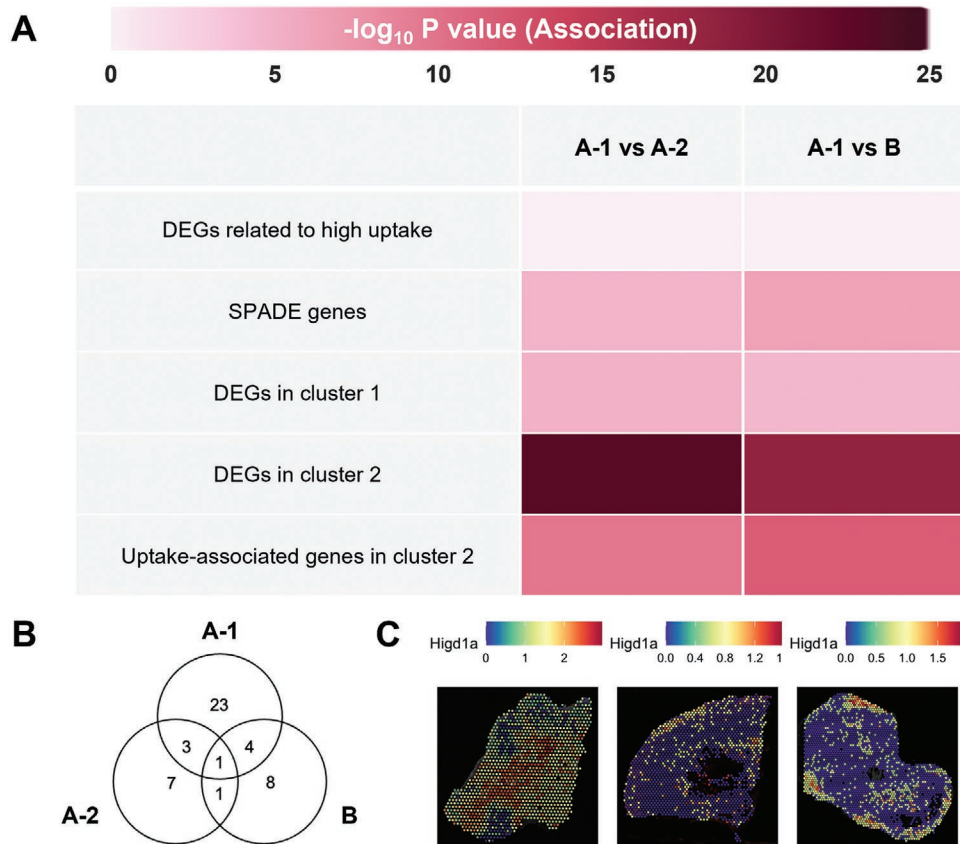


Figure 7. Results of ST validation study. A) A table of a statistical testing for each item. Fisher's exact test, which tests the null hypothesis that the given two sets are independent of each other, was performed for each item. A p -value of less than 0.05 means that there is a lack of independence between the two sets, so it can indicate an association between the sets. For example, in the item of "Uptake-associated genes in cluster 2" between Sample A-1 and Sample B, out of a total of 32 285 genes, 31 genes in Sample A-1, 14 genes in Sample B, and 5 common genes between them were found, resulting in $-\log_{10} p\text{-value} = 11.94$. The p -value is expressed on a color scale. B) A Venn diagram of uptake-associated genes in cluster 2 demarcated by Sample A-1, Sample A-2, and Sample B. C) Spatial feature plots with 3 ST datasets on only one common gene, *Higd1a*.

the other from another 4T1 tumor-bearing mouse (Sample B). By addressing the former and the latter dataset, we assumed that the molecular markers obtained from the first sample were tested under intratumoral heterogeneity and intertumoral heterogeneity for each. Division of uptake pattern clusters, CellDART analysis, and subgroup fluorescence analysis were processed the same as Sample A-1 (Figures S8–S13, Tables S6 and S7, Supporting Information). When investigating the degree of association for each gene set term (e.g., uptake-associated genes in cluster 2), we could find a statistically significant association between Sample A-1 and Sample A-2 or between Sample A-1 and Sample B (Figure 7). Similar to Sample A-1, the uptake-associated genes in cluster 2 included genes related with hypoxia in Sample A-2 (Table S6, Supporting Information) and glycolysis, hypoxia, and apoptosis in Sample B (Table S7, Supporting Information). Also, there were common genes in uptake-associated genes in cluster 2 from different samples. Especially, *Higd1a* was an uptake-associated gene in all three samples. *Higd1a* is one of the markers for tumor hypoxia and regulates cellular reactive oxygen species and oxygen consumption to enhance cancer cell survival.^[31] Also, when drawing spatial feature plots of *Higd1a*, the spatial patterns of

the gene were well matched with the fluorescence images of PEGylated liposomes (Figure 7C). In addition, merged scores of hypoxia, glycolysis, and apoptosis can well represent the intratumoral uptake pattern of PEGylated liposomes (Figure S14 and Table S8, Supporting Information).

Heterogeneity in EPR-mediated nanomedicine delivery is considered to be a cause of heterogeneous outcomes in clinical trials of nanomedicines. To improve clinical outcomes, predictive biomarkers for the EPR effect should be established. Therefore, molecular markers to predict the efficiency of EPR are urgently needed to design successful clinical trials. Currently, several methods are suggested as EPR markers, including companion imaging biomarkers using radiolabeled nanoparticles and serum markers related to tumor stroma.^[32] We believe that the molecular markers found by our platform can be used as precise EPR markers after validation in other types of cancer models. After the validation steps, the EPR markers can be used as predictive biomarker for the nanomedicine. Also, the molecular markers found in this study can be utilized to enhance the EPR effect using a gene-drug interaction database. For example, integrative LINCS database (<http://www.ilincs.org/ilincs/>) provides a list of small-molecule drugs that enhance or

inhibit the molecular process when the molecular markers are provided. The enhancer identified by the database can be used to enhance the EPR effect of the nanomedicine. Taken together, the molecular markers found by the platform here may provide potential to optimize the precise utilization of nanomedicines by predicting the EPR effect and finding EPR enhancers for the nanomedicines.

In this study, we tested only one example nanomedicine in one tumor model, PEGylated liposome and 4T1 tumor model, respectively. The tissue distribution of a nanomedicine can be affected by materials, surface modifications, and possibly by internal drug loads. Therefore, the result from this study cannot be generalized to other types of nanomedicine. However, if there is a target nanomedicine and target cancer tissue, this new method can then be used to optimize the component and surface chemistry of the nanomedicine to obtain a better tissue distribution pattern. In addition, a temporal approach should be investigated later for more accurate conclusions.

3. Conclusion

Herein, we developed a molecular marker identification platform for nanomedicine distributions by integrating ST data and fluorescence nanomedicine distribution imagery. The molecular markers related to hypoxia, glycolysis, and apoptosis are associated with the intratumoral distribution of PEGylated liposomes. An interdisciplinary approach including image processing, an artificial intelligence-algorithm-based gene analysis, biological annotations, and flexible interpretations of complicated mass transfer events were all involved in the development of the marker identification platform. We believe that this platform can be applied to a variety of tissues and other types of drugs, such as peptides, antibodies, and antibody drug conjugates, for the exploration of novel molecular markers related to drug distributions. Moreover, the use of molecular markers can enhance the precise utilization of drug candidates.

4. Experimental Section

Materials: 1,2-Distearoyl-*sn*-glycero-3-phosphocholine (DSPC), cholesterol, 1,1'-dioctadecyl-3,3',3'-tetramethylindocarbocyanine perchlorate were purchased from Sigma-Aldrich, Korea. 1,2-Distearoyl-*sn*-glycero-3-phosphoethanolamine conjugated polyethylene glycol (DSPE-PEG) was purchased from Creative PEGworks. Avanti Mini Extruder was purchased from Avanti Polar Lipids. The rabbit anti-VDAC1 antibody (ab154856, abcam), rat anti-PECAM-1 antibody (14-0311-82, Invitrogen), Alexa Fluor 488 conjugated goat anti-rabbit IgG secondary antibody (A11034, Invitrogen), and Alexa Fluor 647 conjugated goat anti-rat IgG secondary antibody (A21247, Invitrogen) were used for immunofluorescence.

Synthesis and Characterization of Dil-Loaded Liposomes: Size and PEGylation controlled liposomes were synthesized by extrusion method with Avanti mini extruder. The liposomes were composed of DSPC, DSPE-PEG, cholesterol, and Dil fluorescent dye ($\lambda_{ex} = 553$ nm, $\lambda_{em} = 570$ nm). The ratio of DSPC and DSPE-PEG was regulated for synthesizing high PEGylated liposome and low PEGylated liposome. Thin-film lipids were prepared by vaporizing organic solvents and hydrated by distilled water. Hydrated fluorescent liposome layers were extruded using 400 and 200 nm pore size membrane filters to make a large size liposome. Smaller sized liposome was formed by extrusion using 400, 200, 100 nm pore size

membrane in order. The hydrodynamic size of Dil-loaded liposomes was about 292 nm in a dynamic light scattering instrument (DLS).

4T1 Breast Cancer Model and Fluorescence Imaging: To prepare a 4T1 syngeneic tumor model, 4T1 breast cancer cells (10^6 cells/0.02 mL) were injected subcutaneously into the BALB/c mice at the right thigh region. After 10 days, Dil-loaded liposomes were injected intravenously. In vivo fluorescence imaging was performed at 0, 4, and 24 h after injection using in vivo imaging system. For the verification of liposome distribution in organs, mice were sacrificed 24 h after injection. The main organs (heart, lung, kidney, liver, spleen, muscle, and tumor) were collected and observed by in vivo imaging system for fluorescence imaging.

Acquisition of Spatial Transcriptomics (ST) Library, H&E Staining Image, and Fluorescence Image: Fresh tumor samples were embedded in the mold with optimal cutting temperature (OCT) compound for cryo-sectioning. ST library was acquired by several steps: cryo-sectioning, fixation, permeabilization, cDNA synthesis, and RNA sequencing. All the methods were carried out in the way that 10x Genomics visium protocol recommended. The fresh tissue samples were embedded in OCT compound (25608-930, VWR, USA). Consecutive tissue slices were prepared, which were used for H&E staining, ST library, and fluorescence imaging. The slices were acquired by thin blades used in cryotome so that the fluorescence pattern affected by gene expression could be explored thoroughly. The tissue section for ST were placed on Visium slides (both Visium Tissue Optimization Slides, 1 000 193, 10X Genomics, USA and Visium Spatial Gene Expression Slides, 1 000 184, 10X Genomics). The fixation was performed under the recommended protocol using chilled methanol. The cDNA libraries were prepared and sequenced on a NovaSeq 6000 System S1200 (Illumina, USA) at a sequencing depth up to 250 m read-pairs.

Raw FASTQ files and H&E images were processed by sample with the Space Ranger v1.1.0 software. The process uses STAR v2.5.1b (Dobin et al., 2013) for genome alignment, against the Cell Ranger (mouse mm10 reference package). The process was performed by "spaceranger count" command.

When acquiring a fluorescent image, the parameters were modified to avoid the saturation of signal. After acquiring the raw fluorescent image, the image was normalized by setting the maximum fluorescence value at normal tissue to 0 and the maximum fluorescence value of the tissue treated with fluorescent nanoparticles to 1. To avoid confusion in terms, "pixel" was used only in the fluorescence image and "spot" was used only in the spatial transcriptomics profile. Also, all the following analysis procedures were summarized (Table 1).

Image Registration: To fit the shape of the acquired fluorescence image to the spatial transcriptomics spots, the image registration process based on symmetric diffeomorphic registration^[33] implemented by Python-based open-source DiPY package. The fluorescence image was changed to gray-scale using opencv2 package. For the registration, linear rigid transformation was performed after the matching center of masses of both images. The rigid and affine transformation processes were optimized using mutual information between two gray-scale images. After the linear transformation, nonlinear warping process based on symmetric diffeomorphic registration algorithm was performed using function "SymmetricDiffeomorphicRegistration" with "CCMetric" for optimization. The transformed image was visually evaluated.

Annotation of Distance in Spatial Transcriptomics Spots: It is come up with the distance from the surface of the tumor and defined the distance of spots in the left-boundary region as 0. As the distance was raised one by one, the next layer was immediately marked. The map was then colored differently depending on the distance. The fluorescence intensity values mapped to the spots were averaged for each distance and a plot showing the relationship between the distance and the average fluorescence intensity was created.

Mathematical Simulation of Diffusion: When illustrating dynamics of diffusion, Fick's law is used typically as follows

$$\frac{\partial C}{\partial t} + u \frac{\partial C}{\partial x} + v \frac{\partial C}{\partial y} + w \frac{\partial C}{\partial z} = D \left\{ \frac{\partial^2 C}{\partial x^2} + \frac{\partial^2 C}{\partial y^2} + \frac{\partial^2 C}{\partial z^2} \right\} + R \quad (1)$$

Table 1. Summary of the analysis procedures.

Step 1. Modification of the fluorescence image		
Python-based open-source DiPY package		
Step 2. Modification of the spatial transcriptomics library		
All the spots with RNA reads less than 500 (A-1) or 100 (A-2, B) were neglected.		
In this condition, all the spots had the mitochondrial percent < 25% and the hemoglobin percent < 20%.		
Step 3. Acquisition of marker genes		
	DEG analysis	SPADE algorithm
# of steps	3; high-uptake spots configuration → DEG acquisition → correlation analysis	1; SPADE algorithm
Spot value	The average of fluorescence intensities of spot-size patches	Principal components of features extracted from VGG16
Association	Pearson correlation coefficient	Empirical Bayes algorithm and linear regression analysis
p-value	Wilcoxon rank sum test for uptake cluster DEGs; Linear regression analysis for uptake-associated genes	Empirical Bayes algorithm and linear regression analysis for SPADE genes
Step 4. Acquisition of uptake clusters		
	Combination of VGG16 and K means clustering	
Mechanism	Texture recognition	
# of steps	3; high-uptake spots configuration → VGG16 & K means clustering (K = 4 for Sample A-1, A-2; K = 6 for Sample B) → acquisition of uptake-clusters	

where \mathbf{C} is concentration vector, (u, v, w) is velocity vector, D is diffusivity, and R is source or sink term. Two assumptions are put to simulate the result of the formula. At first, that the number of gaps of blood vessels is proportional to the expression level of *Pecam1* gene is anticipated. And it was thought the tissue sample was close to the median plane of the whole tumor, so it got

$$w = 0, \frac{\partial \mathbf{C}}{\partial z} = 0 \quad (2)$$

(u, v, w) was regarded as null vector according to the literature.^[10] Briefly, when assuming cylindrical blood vessels perpendicular to the median plane, the fluid velocity at the edge of each spot can be induced by the experimentally estimated values

$$\begin{aligned} L(\text{Spot diameter}) &= 100 \mu\text{m} \\ H(\text{Spot height}) &[\mu\text{m}] \\ S(\text{Surface area of blood vessels per unit volume of tissue}) &= 0.0034 \mu\text{m}^2 / \mu\text{m}^3 \\ n(\text{Number of gaps per unit area of blood vessel}) &= 500 \text{ gaps mm}^{-2} \\ V(\text{Experimentally estimated flow rate}) &= 0.065 \mu\text{m}^3 \text{s}^{-1} \text{gap} \\ V_{\text{edge}}(\text{Fluid velocity at the edge of each spot}) &[\mu\text{m s}^{-1}] \\ \therefore \pi \times L \times H \times V_{\text{edge}} &= \frac{\pi}{4} \times L^2 \times H \times S \times n \times V \end{aligned} \quad (3)$$

The result of $V_{\text{edge}} = 2.7625 \times 10^{-6} \mu\text{m s}^{-1}$ indicated that the fluid velocity could not even account for the movement of nanoparticles in a single micrometer over 24 h.

Thus, a numerical approach was used to comprehend the effects of the concentration gradient in the absence of the flow rate

$$\begin{aligned} \frac{\mathbf{C}^{t+\Delta t}(x, y) - \mathbf{C}^t(x, y)}{\Delta t} &= D \left\{ \frac{\mathbf{C}^t(x + \Delta x, y) + \mathbf{C}^t(x - \Delta x, y) - 2\mathbf{C}^t(x, y)}{(\Delta x)^2} \right\} \\ &+ D \left\{ \frac{\mathbf{C}^t(x, y + \Delta y) + \mathbf{C}^t(x, y - \Delta y) - 2\mathbf{C}^t(x, y)}{(\Delta y)^2} \right\} \\ &+ k \times \text{Expression} \end{aligned} \quad (4)$$

where Δx and Δy were set to be the same. And various simulation results of Fick's diffusion annotated by \mathbf{C}/k with different $D/\Delta x^2$ values and numbers of replications were explored.

Differentially Expressed Genes Based on Fluorescence Intensity: Image binarization was performed to analyze the fluorescence image pixels combined with the spots with transcriptomic data. Spots with high fluorescence (high-uptake spots) were distinguished from spots with low fluorescence (low-uptake spots) by dichotomy. When making a binary image, only pixels with a brightness greater than 25% of the maximum fluorescence intensity were selected as high pixels. The fluorescence intensity was measured and analyzed by ImageJ (ver 1.8; <https://imagej.nih.gov/ij/download.html>). Once the binary image was acquired, the binary map was then created in search of the pixel values (i.e., 0 or 1) corresponding to the centers of the spots.

To visualize the spots according to gene features, t-distributed stochastic neighbor embedding (t-SNE) was employed using the Seurat package (version 4.0.5) in R. Spots with RNA reads less than 500 were excluded for the following analyses. The perplexity of *RunTSNE* was set to 30. DEGs between high-uptake spots and low-uptake spots were explored by Wilcoxon rank sum test on *FindMarkers* in Seurat package with default parameters. Finally, DEGs were sorted by fold change (FC).

Identification of Genes Associated with Image Features: In addition to the overall DEG analysis, another approach, spatial gene expression patterns by deep learning of tissue images (SPADE), was used.^[19] A pre-trained VGG16 model extracted 512 features per patch around each spot and principal component analysis (PCA) was performed to reduce dimensions of features. Top three principal components (PCs) were selected to identify SPADE genes. SPADE genes in each PC were discovered on empirical Bayes algorithm and linear regression analysis. Genes were then sorted by FC.

For visualizing image feature-associated genes, *EnhancedVolcano* function was used with pCutoff of 0.05 and FCcutoff of 0.3. Top 1000 genes with FDRs below 0.05 were selected, and spatial feature plots of top genes with highest FC were represented. For GO analysis, *enrichGO* function was used and p values were adjusted by Benjamini-Hochberg (B&H) method. GO analysis was performed according to biological process (BP), cellular component (CC), and molecular function (MF) using top 30 up-regulated or down-regulated genes. When specifying biological annotations, g:Profiler (<https://biit.cs.ut.ee/gprofiler/gost>) was used instead of *enrichGO* function.

Subgroup Fluorescence Analysis: The fluorescence image was split into 394×384 patches of 5×5 patch size and extracted 512 features per each patch by using the VGG16 model. And then patches were classified by K means clustering according to the features with K of 4. As a result, the fluorescence image was separated into 4 regions of interest (ROIs) according to the texture. Then, the binary map was merged into 2 notable ROIs out of 4. As a result, high-uptake spots were separated into 2 clusters and the other spots were allocated to default 0. In conclusion, 3 clusters were formed totally. Outliers of each uptake cluster were defined as incoherent spots between the uptake pattern clusters and newly formed clusters by unsupervised hierarchical clustering of spots in cluster 1 and 2. The outliers were then eliminated for further analyses. DEGs representing each uptake clusters were generated by comparison to the default cluster using *FindMarkers* in R.

Analysis of Cell Types Associated with Fluorescence Distribution: Multimodal intersection analysis (MIA) was performed to comprehend which cell type was relevant to each uptake cluster.^[21] Single-cell RNA sequencing (scRNA-seq) dataset was obtained from the previous research of 4T1 tumor model.^[34] Marker genes in each cell type were

determined with adjusted p -value $< 10^{-5}$ in Wilcoxon rank-sum test from *FindMarkers*. Also, marker genes in each uptake cluster were determined similarly, except for adjusted p -value < 0.01 instead of adjusted p -value $< 10^{-5}$. Afterward, each common set of genes in a specific cell type and a specific spatial region was acquired, and only enrichment was represented. Finally, all the common sets of genes were analyzed using hypergeometric cumulative distribution to figure out which cell type was significantly characteristic to which spatial region.

Other cell-type matching algorithms were addressed for verification. Robust cell type decomposition (RCTD) was used to determine the distribution of each cell type through supervised maximum likelihood estimation as a representative alternative method for MIA analysis.^[22] All the parameters were set to the default settings including *doublet_mode* of “doublet” in run.RCTD. Another algorithm, CellDART,^[23] which used adversarial domain adaptation classification from single-cell data with pre-labeled cell types was additionally performed to find cell types related to the distribution of fluorescence. When implementing RCTD and CellDART, the same scRNA-seq dataset with MIA analysis was used.

Genes Correlated with Fluorescence Intensity of Subclusters Defined by the Image: To acquire uptake-associated genes from uptake DEGs, Pearson correlation coefficient was calculated. The expression of the gene and the fluorescence intensity within each uptake cluster was correlated. To assess a statistical significance of the relationship between the fluorescence intensity and the gene expression, the slope of the regression curve was analyzed. Only genes with p value less than 0.05 were sorted according to the correlation coefficient. The resultant uptake-associated genes were explored with gene ontology analysis. The uptake-associated genes were robustly calculated regardless of the criteria for obtaining fluorescence intensities (max, mean+2s.d., mean+1s.d., mean, median, min, etc.), so it was decided to calculate it by averaging pixels in spot-size patches without further justification. In sum, two-step approach was used, DEG identification at first and correlation analysis later, because unreliable genes easily came up, if only correlation analysis was performed.

Validation of the Uptake-Associated Markers with Immunofluorescence Experiment: To validate the first-ranked liposome uptake associated molecular marker from the analysis above, the primary anti-VDAC1 and anti-PECAM-1 antibodies were treated on the methanol fixed frozen tumor tissues from fluorescent liposome injected 4T1 tumor-bearing mice. Afterward, fluorescent secondary anti-IgG antibody was treated, and the IF images were acquired by confocal microscopy (STELLARIS 5, Leica microsystems). The microscope scale was set to 100x and 400x for evaluating the overall and the local distribution of antibodies and liposomes. After obtaining IF images, Pearson correlation coefficient between an IF image of an antibody and a distribution of fluorescent liposomes was calculated.

Validation of the Uptake-Associated Markers with Another ST Datasets: To verify the molecular markers from the first ST data (Sample A-1), two more ST datasets were acquired, one of which was from the same tumor (Sample A-2) and the other of which was from another 4T1 tumor-bearing mouse (Sample B). At first, spots with RNA reads less than 100 instead of 500 were excluded for the following analyses. Basic analyses including plotting RNA reads, spatial clustering, representation of DEGs of each cluster were performed. And then, CellDART analysis and subgroup fluorescence analysis followed. In subgroup fluorescence analysis, K was set as the minimum requirement for the division of the surface area from the inner area. In Sample A-2, K was set to 4; on the other hand, K was set to 6 in Sample B. To test the association between Sample A-1 and Sample A-2 or between Sample A-1 and Sample B for each gene set term, Fisher's exact test can be used to assess the association of identified gene sets between the different samples.^[21,35]

Statistical Analysis: DEGs were explored by Wilcoxon rank sum test on *FindMarkers* in Seurat package. DEGs were validated by Fisher's exact test between different datasets. p -values were adjusted by B&H method. GO was performed by *enrichGO* function and *g:Profiler*. Association between two variables was explored by Pearson correlation coefficient

and regression analysis. Dimension reduction was conducted by PCA and t-distributed stochastic neighbor embedding (tSNE). Clustering was performed by K means clustering and unsupervised hierarchical clustering. Image features were extracted by VGG16 model merged with PCA assay. All the values were expressed by mean \pm standard deviation (SD). All the adjusted p values less than 0.05 were considered significant. Statistical analysis and the image processing procedures were performed using R 4.0.2 and Python 3.7. All the packages and the pipelines followed the default parameters, and all the analyses were based on Sample A-1 unless otherwise specified.

Ethical Statement: The animal experiments performed for this study were approved by the Woojung Bio IACUC, the Republic of Korea. The approval code is IACUC2001-003. There is no other issue in animal experiment ethics compliance.

Supporting Information

Supporting Information is available from the Wiley Online Library or from the author.

Acknowledgements

This study was supported by the National Research Foundation of Korea (NRF) (Nos. NRF-2019M2D2A1A01058210, NRF-2020R1C1C1009000, 2020M3A9B6038086, and 2021M2E8A1039564) and Creative-Pioneering Researchers Program through Seoul National University (SNU).

Conflict of Interest

J.P. and J.C. are researchers in Portrai. H.C. is the co-founder and the Chief Technology Officer of Portrai and a scientific advisor of AltheNutrigene, Inc. H.-J.I. is the co-founder and the Chief Scientific Officer of Portrai. H.-J.I. is a consultant of Cellbion. Otherwise, there is no competing financial interest.

Author Contributions

J.P. and J.C. contributed equally to this work. H.-J.I. and H.C. designed this project. Experiments regarding liposome synthesis, cell, and mouse were performed by J.C. and J.P. J.L. especially supported the validation experiments. Spatial transcriptomics and imaging analysis were performed by J.P., J.C., and H.C. The manuscript is written by J.P., J.C., and H.-J.I. All authors have contributed to the completion of manuscript.

Data Availability Statement

The data that support the findings will be available in Gene Expression Omnibus at GSE196506 following an embargo from the date of publication to allow for commercialization of research findings.

Keywords

apoptosis, enhanced permeability and retention, glycolysis, hypoxia, lipid nanoplateforms, molecular markers, spatial transcriptomics

Received: August 26, 2022
Published online:

- [1] J. Shi, P. W. Kantoff, R. Wooster, O. C. Farokhzad, *Nat. Rev. Cancer* **2017**, *17*, 20.
- [2] D. M. Smith, J. K. Simon, J. R. Baker Jr, *Nat. Rev. Immunol.* **2013**, *13*, 592.
- [3] C. N. Fries, E. J. Curvino, J. L. Chen, S. R. Permar, G. G. Fouda, J. H. Collier, *Nat. Nanotechnol.* **2021**, *16*, 1.
- [4] M. J. Mitchell, M. M. Billingsley, R. M. Haley, M. E. Wechsler, N. A. Peppas, R. Langer, *Nat. Rev. Drug Discovery* **2021**, *20*, 101.
- [5] Y. Barenholz, *J. Controlled Release* **2012**, *160*, 117.
- [6] M. Yu, J. Zheng, *ACS Nano* **2015**, *9*, 6655.
- [7] a) C. G. England, H.-J. Im, L. Feng, F. Chen, S. A. Graves, R. Hernandez, H. Orbay, C. Xu, S. Y. Cho, R. J. Nickles, Z. Liu, D. S. Lee, W. Cai, *Biomaterials* **2016**, *100*, 101; b) M. Jeon, G. Kim, W. Lee, S. Baek, H. N. Jung, H.-J. Im, *J. Nanobiotechnol.* **2021**, *19*, 262.
- [8] a) Y. Shi, R. van der Meel, X. Chen, T. Lammers, *Theranostics* **2020**, *10*, 7921; b) J. Fang, H. Nakamura, H. Maeda, *Adv. Drug Delivery Rev.* **2011**, *63*, 136.
- [9] M. Bolkestein, E. de Blois, S. J. Koelewijn, A. M. M. Eggermont, F. Grosveld, M. de Jong, G. A. Koning, *J. Nucl. Med.* **2016**, *57*, 601.
- [10] S. Sindhvani, A. M. Syed, J. Ngai, B. R. Kingston, L. Maiorino, J. Rothschild, P. MacMillan, Y. Zhang, N. U. Rajesh, T. Hoang, J. L. Y. Wu, S. Wilhelm, A. Zilman, S. Gadde, A. Sulaiman, B. Ouyang, Z. Lin, L. Wang, M. Egeblad, W. C. W. Chan, *Nat. Mater.* **2020**, *19*, 566.
- [11] K. Yokoi, M. Kojic, M. Milosevic, T. Tanei, M. Ferrari, A. Ziemys, *J. Cancer Res.* **2014**, *74*, 4239.
- [12] G. Song, D. B. Darr, C. M. Santos, M. Ross, A. Valdivia, J. L. Jordan, B. R. Midkiff, S. Cohen, N. Nikolaishvili-Feinberg, C. R. Miller, T. K. Tarrant, A. B. Rogers, A. C. Dudley, C. M. Perou, W. C. Zamboni, *Clin. Cancer Res.* **2014**, *20*, 6083.
- [13] X. Li, C.-Y. Wang, *Int. J. Oral Sci.* **2021**, *13*, 36.
- [14] a) V. Marx, *Nat. Methods* **2021**, *18*, 9; b) A. Rao, D. Barkley, G. S. França, I. Yanai, *Nature* **2021**, 596, 211.
- [15] a) O. S. Wolfbeis, *Chem. Soc. Rev.* **2015**, *44*, 4743; b) M. Funovics, X. Montet, F. Reynolds, R. Weissleder, L. Josephson, *Neoplasia* **2005**, *7*, 904.
- [16] M. Bolkestein, E. de Blois, S. J. Koelewijn, A. M. Eggermont, F. Grosveld, M. de Jong, G. A. Koning, *J. Nucl. Med.* **2016**, *57*, 601.
- [17] K. Pal, V. S. Madamsetty, S. K. Dutta, D. Mukhopadhyay, *Int. J. Nanomed.* **2019**, *14*, 5109.
- [18] J. Kalucka, L. P. M. H. de Rooij, J. Goveia, K. Rohlenova, S. J. Dumas, E. Meta, N. V. Conchinha, F. Taverna, L.-A. Teuwen, K. Veys, M. García-Caballero, S. Khan, V. Geldhof, L. Sokol, R. Chen, L. Treps, M. Borri, P. de Zeeuw, C. Dubois, T. K. Karakach, K. D. Falkenberg, M. Parys, X. Yin, S. Vinckier, Y. Du, R. A. Fenton, L. Schoonjans, M. Dewerchin, G. Eelen, B. Thienpont, et al., *Cell* **2020**, *180*, 764.
- [19] S. Bae, H. Choi, D. S. Lee, *Nucl. Acids Res.* **2021**, *49*, e55.
- [20] Y. Zhou, G. Luo, *Clin. Transl. Oncol.* **2020**, *22*, 1952.
- [21] R. Moncada, D. Barkley, F. Wagner, M. Chiodin, J. C. Devlin, M. Baron, C. H. Hajdu, D. M. Simeone, I. Yanai, *Nat. Biotechnol.* **2020**, *38*, 333.
- [22] D. M. Cable, E. Murray, L. S. Zou, A. Goeva, E. Z. Macosko, F. Chen, R. A. Irizarry, *Nat. Biotechnol.* **2022**, *40*, 517.
- [23] S. Bae, K. J. Na, J. Koh, D. S. Lee, H. Choi, Y. T. Kim, *Nucleic Acids Res.* **2022**, *50*, e57.
- [24] a) W. J. Brownlee, F. P. Seib, *Sci. Rep.* **2018**, *8*, 12318; b) M. Neshatian, S. Chung, D. Yohan, C. Yang, D. B. Chithrani, *J. Biomed. Nanotechnol.* **2015**, *11*, 1162.
- [25] K. O. Alfarouk, *J. Enzyme Inhib. Med. Chem.* **2016**, *31*, 859.
- [26] J. G. Rajendran, D. A. Mankoff, F. O'Sullivan, L. M. Peterson, D. L. Schwartz, E. U. Conrad, A. M. Spence, M. Muzi, D. G. Farwell, K. A. Krohn, *Clin. Cancer Res.* **2004**, *10*, 2245.
- [27] A. E. Greijer, E. van der Wall, *J. Clin. Pathol.* **2004**, *57*, 1009.
- [28] J. Castellano, R. Aledo, J. Sendra, P. Costales, O. Juan-Babot, L. Badimon, V. Llorente-Cortés, *Arterioscler., Thromb., Vasc. Biol.* **2011**, *31*, 1411.
- [29] J. C. Perman, P. Boström, M. Lindborn, U. Lidberg, M. StÅhlman, D. Hägg, H. Lindskog, M. Scharin Täng, E. Omerovic, L. Mattsson Hultén, A. Jeppsson, P. Petursson, J. Herlitz, G. Olivecrona, D. K. Strickland, K. Ekroos, S. O. Olofsson, J. Borén, *J. Clin. Invest.* **2011**, *121*, 2625.
- [30] Z. Zhou, M. Christofidou-Solomidou, C. Garlanda, H. M. DeLisser, *Angiogenesis* **1999**, *3*, 181.
- [31] K. Ameri, A. Jahangiri, A. M. Rajah, K. V. Tormos, R. Nagarajan, M. Pekmezci, V. Nguyen, M. L. Wheeler, M. P. Murphy, T. A. Sanders, S. S. Jeffrey, Y. Yeghiazarians, P. F. Rinaudo, J. F. Costello, M. K. Aghi, E. Maltepe, *Cell Rep.* **2015**, *10*, 891.
- [32] a) S. K. Golombek, J.-N. May, B. Theek, L. Appold, N. Drude, F. Kiessling, T. Lammers, *Adv. Drug Delivery Rev.* **2018**, *130*, 17; b) K. Yokoi, T. Tanei, B. Godin, A. L. van de Ven, M. Hanibuchi, A. Matsunoki, J. Alexander, M. Ferrari, *Cancer Lett.* **2014**, *345*, 48.
- [33] B. B. Avants, C. L. Epstein, M. Grossman, J. C. Gee, *Med. Image Anal.* **2008**, *12*, 26.
- [34] A. Sebastian, N. R. Hum, K. A. Martin, S. F. Gilmore, I. Peran, S. W. Byers, E. K. Wheeler, M. A. Coleman, G. G. Loots, *Cancers* **2020**, *12*, 1307.
- [35] N. C. Sheffield, C. Bock, *Bioinformatics* **2015**, *32*, 587.